



Deposited via The University of Leeds.

White Rose Research Online URL for this paper:

<https://eprints.whiterose.ac.uk/id/eprint/192276/>

Version: Accepted Version

Article:

Li, Z, Zhang, YG, Torres, M et al. (2023) Neogene burial of organic carbon in the global ocean. *Nature*, 613 (7942). pp. 90-95. ISSN: 0028-0836

<https://doi.org/10.1038/s41586-022-05413-6>

© The Author(s), under exclusive licence to Springer Nature Limited 2023. This is an author produced version of an article published in *Nature*. Uploaded in accordance with the publisher's self-archiving policy.

Reuse

Items deposited in White Rose Research Online are protected by copyright, with all rights reserved unless indicated otherwise. They may be downloaded and/or printed for private study, or other acts as permitted by national copyright laws. The publisher or other rights holders may allow further reproduction and re-use of the full text version. This is indicated by the licence information on the White Rose Research Online record for the item.

Takedown

If you consider content in White Rose Research Online to be in breach of UK law, please notify us by emailing eprints@whiterose.ac.uk including the URL of the record and the reason for the withdrawal request.



1 Neogene burial of organic carbon in the global ocean

2

3

4

5

6

7

8

9 Ziye Li^{1,2,3}, Yi Ge Zhang^{2*}, Mark Torres⁴ and Benjamin J. W. Mills⁵

10

11 ¹College of Marine Geosciences, Ocean University of China, Qingdao, 266100, China

12 ²Department of Oceanography, Texas A&M University, College Station, TX 77843, USA

13 ³MARUM-Center for Marine Environmental Sciences, University of Bremen, 28359 Bremen,
14 Germany

15 ⁴Department of Earth Science, Rice University, Houston, TX 77005, USA

16 ⁵School of Earth and Environment, University of Leeds, Leeds, LS2 9JT, UK

17

18 *Corresponding Author.

19 Department of Oceanography, Texas A&M University, TX 77843, USA

20 yige.zhang@tamu.edu

21

22 **Organic carbon buried in marine sediment serves as a net sink for atmospheric**
23 **carbon dioxide and a source of oxygen^{1,2}. The rate of organic carbon burial through**
24 **geologic history is conventionally established by using the mass balance between**
25 **inorganic and organic carbon, each with distinct carbon isotopic values ($\delta^{13}\text{C}$)^{3,4}. This**
26 **method is complicated by large uncertainties, however, and has not been tested with**
27 **organic carbon accumulation data^{5,6}. Here we report a “bottom up” approach for**
28 **calculating the rate of organic carbon burial that is independent from mass balance**
29 **calculations. We use data from 81 globally distributed sites to establish the history of**
30 **organic carbon burial during the Neogene (~23– 3 million years ago). Our results show**
31 **larger spatiotemporal variability of organic carbon burial than previously estimated^{7,8},**
32 **⁹. Globally, the burial rate is high towards the early Miocene and Pliocene and lowest**
33 **during the mid-Miocene, with the latter period characterised by the lowest ratio of**
34 **organic-to-carbonate burial rates. This is in contrast to earlier work that interpreted**
35 **enriched carbonate ^{13}C values of the mid-Miocene as massive organic carbon burial (i.e.**
36 **the Monterey Hypothesis)^{10,11}. Suppressed organic carbon burial during the warm mid-**
37 **Miocene is probably related to temperature-dependent bacterial degradation of organic**
38 **matter^{12,13}, suggesting that the organic carbon cycle acted as positive feedback of past**
39 **global warming, with implications for our future.**

40

41

42 In the long-term carbon cycle, carbon dioxide is added to the surficial system through
 43 volcanic and metamorphic degassing and the weathering of sedimentary carbon, and is
 44 removed through the deposition of carbonates following chemical weathering of Ca-Mg silicate
 45 rocks and the burial of organic carbon (OC). The buried OC in marine sediment, on average
 46 only 0.1% of the primary production, is effectively isolated from the Earth's surficial system
 47 and therefore serves as a net sink for atmospheric CO₂, a source for O₂, and largely contributed
 48 to the occurrence of fossil fuels (Ref^{1,2}).

49 Traditionally, the fraction of carbon buried as organic carbon (f_{org}) is estimated through
 50 "top-down" isotopic mass balance approaches. The rationale is that there is a large carbon
 51 isotope fractionation associated with photosynthesis, which allows the carbon isotope signature
 52 of marine carbonates ($\delta^{13}\text{C}_{\text{IC}}$) to be used for calculating the fraction of organic vs. inorganic
 53 carbon in the total burial flux^{3,4,6}. Assuming a steady state wherein the isotopic composition
 54 of carbon input to and output from the surficial system are balanced, then

$$55 C_{in} \times \delta^{13}\text{C} = C_{out} \times \delta^{13}\text{C}, \quad \text{Equation 1}$$

$$56 \delta^{13}\text{C}_{in} = \delta^{13}\text{C}_{org} \times f_{org} + \delta^{13}\text{C}_{\text{IC}} \times (1 - f_{org}) \quad \text{Equation 2}$$

57 It is often assumed that the average isotopic composition of carbon input ($\delta^{13}\text{C}_{in}$) is
 58 constant and approximately equal to mantle-sourced volcanic outgassing (-6‰ ± 1‰)¹⁴. Thus,
 59 the portion of carbon buried as organic matter (f_{org}) can be simply calculated if the $\delta^{13}\text{C}_{org}$ and
 60 $\delta^{13}\text{C}_{\text{IC}}$ are known. Positive $\delta^{13}\text{C}$ excursions of marine carbonates are commonly interpreted as
 61 enhanced organic carbon burial over carbonates. For example, during the Neogene period (ca.
 62 23-3 million years ago, Ma), the heaviest $\delta^{13}\text{C}_{\text{IC}}$ occurred during the mid-Miocene, which
 63 coincides with the OC-rich shale deposits in California known as the "Monterey Formation".
 64 The famous "Monterey Hypothesis" argues that the $\delta^{13}\text{C}_{\text{IC}}$ maxima roughly 16-14 Ma
 65 represents globally enhanced OC burial and preservation, which led to subsequent CO₂
 66 drawdown, global cooling, and expansion of ice sheets in East Antarctica during the Middle

67 Miocene Climate Transition (~14 Ma)^{10, 11}.

68 However, the assumption of a stable flux of carbon input with constant isotopic values has
69 been challenged. For example, although the chemical weathering of silicate rocks has been
70 extensively studied, changes of the weathering flux of organic-rich black shale, which is largely
71 responsible for the long-term influx of ¹³C-depleted CO₂ into the atmosphere, are largely
72 unconstrained^{15, 16}. Also, depending on the source of the carbon, volcanic and metamorphic
73 CO₂ could vary significantly in its $\delta^{13}\text{C}$ values (-1 to -11 ‰)¹⁷. Lastly, authigenic carbonates
74 formed as a consequence of anaerobic organic matter oxidation and characterized by relatively
75 negative $\delta^{13}\text{C}$ values, would also complicate mass balance calculations^{18, 19}.

76 In this study, we establish the rate of global organic carbon burial over the Neogene period
77 by utilizing measurements of total organic carbon (TOC%) and dry bulk density, alongside well
78 constrained age models, from 81 sites of the International Ocean Discovery Program (IODP,
79 Fig. 1). Further, we employ an algorithm that propagates the data from discrete, individual sites
80 to biogeochemical “provinces” and then eventually, to the global ocean. This novel bottom-up
81 approach is used to build continuous records of regional and global OC burial in the Miocene
82 (~23-5.33 Ma) and Pliocene (~5.33-2.58 Ma) epochs, offering unique insights into the long-
83 term global carbon cycle and the organic sub-cycle over this critical interval that helped shape
84 our modern world.

85 **Spatial variation of OC burial**

86 We screened 1508 IODP sites (Site 1 to Site U1508) and identified 81 sites to establish
87 mass accumulation rates (MARs) of TOC covering either a large portion or the entirety of the
88 past 23 Myr (Fig. 2, Methods). When small temporal gaps were found, data from nearby sites,
89 often drilled during the same expedition, were used to build a composite record (see Methods).
90 MAR of OC at each site relies on reported TOC wt% and dry bulk density of the sediments
91 compiled and calculated from the IODP database, and sedimentation rates calculated from the

92 age-depth relationship of each site. We compared TOC% results obtained from the standard
93 IODP “subtraction” method and the “acidification” method which presumably yields more
94 accurate results, as well as results obtained during different phases of IODP operations (DSDP,
95 ODP and IODP) from nearby sites, which broadly support the robustness of IODP’s TOC%
96 data (Extended Data Fig. 1, 2, Methods). All age models were updated to the GTS2012 (Ref²⁰)
97 timeframe (Methods).

98 The inherent unsteadiness of depositional systems often results in a negative power-law
99 relationship between measurements of sedimentation rate and the amount of time averaged to
100 determine the rate, independent of the sedimentary depositional environment²¹. To evaluate
101 whether our OC burial rates were affected by this “Sadler effect”, we compared the averaging
102 interval (duration of time between tie-points in an age model), sediment accumulation, and OC
103 burial for each record to determine the potential for spurious patterns to arise in our global OC
104 burial flux reconstruction (Methods, Extended Data Fig. 3). These results suggest that our
105 global OC MAR records are largely free of the Sadler effect and therefore represent realistic
106 sedimentary OC burial changes over time.

107 Many factors impact the rate of OC burial, for example, the evolution of primary producers
108 in the ocean and on land²², marine primary and export productivity²³, bottom water oxygen
109 levels and exposure time^{24, 25}, sea-level²⁴, sediment composition²⁶ and accumulation rates²⁷, the
110 evolution of sediment bioturbators²⁸, and the activity of the microbes that break down organic
111 matter¹². Although our data cannot address all potential factors impacting OC burial, the spatial
112 variability of OC burial rates over different time slices of Neogene indicates that the highest
113 OC burial occurs on continental shelves, coastal seas and deep-sea sediment fans, consistent
114 with the notion that enhanced production and preservation at these places contribute to high
115 OC accumulation rates²² (Extended Data Fig. 4).

116 **Temporal variations of the global OC burial**

117 To build global OC burial from 81 discrete records, we utilized an algorithm following a
118 study that explored global OC burial since the last glacial period²⁹. First, the world's ocean was
119 divided into different provinces based on modern biogeochemical zonation. A simplified
120 version of the ecological geography of Longhurst³⁰ was employed, with the caveat that
121 biogeochemical zonation is potentially subject to changes over time (Extended Data Table 1).
122 The definition of Longhurst provinces was based on atmospheric circulation, light, coastlines,
123 water column stratification, chlorophyll content and other environmental factors³⁰ and has been
124 widely applied in marine biogeochemistry studies. We also explored other approaches to define
125 the provinces, for example, the International Hydrographic Organization Sea Areas, and the
126 Fishing Areas by the Food and Agriculture Organization of the United Nations (Methods and
127 Extended Data Fig. 5) to test the sensitivity of the results to different choices of the provincial
128 definition. Second, we obtained the modern global and hence provincial OC burial in marine
129 sediments based on estimates derived from satellite and core-top data³¹ (Extended Data Fig. 6).
130 Third, the 81 individual TOC MAR records were used to construct relative changes of
131 provincial variability of OC burial (Fig. 2). There is at least one, but often more records to
132 represent each province (Extended Data Table 1).

133 An inherent issue of reconstructing global OC burial is the spatial offset between the
134 presumably largest burial flux in shallow waters, and available continuous sedimentary records
135 in relatively deeper waters (> 500 m). Our approach of using individual records from IODP
136 sites to represent provincial OC burial helps to alleviate this problem. Also, most of the
137 sediment load transported by large rivers does not accumulate on the deltaic area over the long
138 term. This is shown by no major seaward growth of the subaerial delta over decades to centuries
139 of the rivers with the highest sediment discharge such as the Ganges-Brahmaputra, Amazon,
140 and Yellow Rivers³². Gravity drives the fine-grained sediment to be transported off the delta
141 and shelf, usually initiated by sediment flux convergence and subsequently supported by wave

142 and current-induced suspension³³. This is exemplified by the Ganges-Brahmaputra River, the
143 world's largest sediment dispersal system, which is highly effective in transporting sediment
144 to the Bengal Fan bypassing the river delta. The suspended sediment can be found throughout
145 the entire 3,000 km long, 1,000 km wide submarine fan³², the record of which is captured by
146 Sites 758 and U1451 in our dataset.

147 Importantly, sedimentary organic matter degrades over time. Studies on the decay of
148 organic matter observed a general relationship between the decomposition rate (k) and age of
149 the sediment (t), given by $\log k = -0.95 \log t - 0.81$ (ref³⁴). This relationship predicts that only
150 ~4% of the original sedimentary OC (100%) is still preserved in one-million-year-old
151 sediments. Since the current data and theory of OC decomposition is limited to the late
152 Pleistocene, this relationship therefore cannot be directly extrapolated to the entire Neogene.
153 Nevertheless, the rate of degradation levels off quickly after a few million years. As a result,
154 we averaged the OC burial data between 2.5-0.5 Ma at each site and defined this as “modern
155 burial” (Extended Data Fig. 6), following the common practice of many carbon cycle studies
156 that treat the Pleistocene mean value as “modern”^{1, 2}. For all IODP sites, their Neogene OC
157 burial variabilities are relative to this “modern” value. As a reference, the modern OC burial in
158 the global ocean is estimated to be 0.15 Gt C yr⁻¹ (Ref³¹).

159 Our calculated OC burial rates for the global ocean (Fig. 3a) exhibit large fluctuations,
160 with the highest fluxes found in the early Miocene and Pliocene, and lowest in the mid-Miocene.
161 The highest OC burial rate in our record (~4 Ma) is about 0.23 ± 0.019 (1σ) Gt C yr⁻¹, which
162 is roughly 1.8 times greater than the lowest OC burial rate, which occurred around ~13.5 Ma
163 and was 0.083 ± 0.011 Gt C yr⁻¹. When cast in terms of the relative rate of OC burial over time,
164 our data suggest variations between about 0.5 and 1.5 times the present-day rate.

165 In contrast, global biogeochemical models predict much smaller variations in OC burial
166 rates. The COPSE model calculates organic fluxes using built-in nutrient cycles⁷, where the

167 oceanic concentrations of phosphate and nitrate control primary productivity and hence OC
168 burial. A different approach is used in GEOCARBSULFOR, which derives organic fluxes from
169 the isotopic records of carbon and sulfur using the isotope mass balance approach detailed
170 earlier (e.g., Eq. 1 and 2)⁸. Both models predict OC burial rate variations within only 10% of
171 the present-day rate, less than one quarter of the actual variation we show, and they tend to
172 predict higher OC burial rates in the mid-Miocene whereas our new record shows a much
173 reduced rate (Fig. 3b). A closer match to our data is seen in the inverse carbon cycle model of
174 Li and Elderfield⁹, which uses the Sr, Os and C isotope systems to back-calculate weathering
175 and burial fluxes. Even though this approach estimates a greater degree of variation in OC
176 burial than the more tightly coupled GEOCARBSULFOR and COPSE models, it is still
177 substantially less than shown in our data (around 0.7 - 0.95 versus our range of around 0.5 -
178 1.5, Fig. 3b).

179 **Reassessing the Neogene carbon cycle**

180 The residence time of dissolved inorganic carbon in the ocean is on the order of 10^5 years³⁵.
181 On longer timescales, a change in the global organic carbon reservoir, arising on account of a
182 persistent change in the proportion of carbon that is stored as organic carbon rather than as
183 carbonate, must induce a shift in the global mean ^{13}C content of the carbonate that is being
184 stored, assuming the input of carbon to the surficial system does not change³⁵. Thus, the long-
185 lasting positive carbon isotope excursion between 17-13.5 Ma (early to middle Miocene) is
186 thought to be related to the Monterey Formation found in California and other widespread
187 organic-rich sediment deposition around the rim of the Pacific Ocean. The lower section of the
188 Miocene Monterey Formation commonly has calcareous facies with abundant mudstones and
189 shales, followed by the mid-Miocene phosphatic facies, which are organic rich and coincide
190 with the positive excursions of benthic $\delta^{13}\text{C}$ (Ref^{36, 37, 38}). This is the basis for the supposition
191 that a large quantity of OC could have been buried during this time. The famous “Monterey

192 Hypothesis" links this enhanced OC burial to the subsequent drop in atmospheric CO₂, global
193 cooling and Antarctica glaciation observed in the middle Miocene climate transition^{11,39}.

194 However, when OC burial rates for the Monterey Formation were quantified from the El
195 Capitan State Beach, where TOC was abundant and varied between 1.2 and 23.2 wt%, average
196 OC burial rate is only 0.23 mg cm⁻² yr⁻¹ between 16.3 -12.7 Ma, with the peak averaged rate of
197 0.39 mg cm⁻² yr⁻¹ found between 14.5 to 13.3 Ma, and the lowest of 0.04 mg cm⁻² yr⁻¹ during
198 13.3-12.7 Ma³⁷. These low accumulation rates are primarily due to low sedimentation rates,
199 such that the OC burial near California is directly comparable with our open ocean sites. For
200 example, in the eastern equatorial Pacific, the average "Monterey period" (17-13.5 Ma) burial
201 rates are 0.14 mg cm⁻² yr⁻¹ at Site 1337 and 0.19 mg cm⁻² yr⁻¹ at Site 1338. When all three records
202 are compared over the same time interval (16.3-12.7 Ma), the Monterey Formation at El
203 Capitan (0.23 mg cm⁻² yr⁻¹) is indistinguishable from the equatorial upwelling region (Site 1338,
204 0.22 mg cm⁻² yr⁻¹), but records much lower burial rates than the deep-sea sedimentary fans (Bay
205 of Bengal, Site U1451, 6.5 mg cm⁻² yr⁻¹, Extended Data Fig. 7). These quantitative analyses
206 further argue against the conclusion that massive OC burial occurred near the Pacific rim during
207 the "Monterey period" and is therefore responsible for the positive $\delta^{13}\text{C}$ excursion.

208 A simple interpretation of the positive $\delta^{13}\text{C}$ excursion recorded in benthic foraminifera
209 (Fig. 4b) during the mid-Miocene (i.e., due to enhanced OC burial) does not consider potential
210 changes in the input of carbon to the surficial system, in terms of both flux and isotopic
211 composition. The $\delta^{13}\text{C}$ of atmospheric CO₂, reconstructed by benthic foraminiferal $\delta^{13}\text{C}$ from
212 regions that presumably maintain close air-sea carbon exchange, i.e., areas with deep-water
213 formation, provides important insights into possible changes in the source of atmospheric CO₂
214 (Ref⁴⁰). During the mid-Miocene, this record exhibits the most positive values (between -5.5
215 and -5‰) of the entire Neogene (Fig. 4c), highlighting the potential contribution of isotopically
216 heavy CO₂ to the atmosphere.

217 Volcanic outgassing of CO₂ represents a more ¹³C-enriched source of atmospheric CO₂ in
218 the long-term carbon cycle relative to OC weathering. During the mid-Miocene, the Columbia
219 River flood basalt erupted in the northwestern United States. This volcanism peaked between
220 17-14.5 Ma^{41,42}. Because of its link to the subducted Farallon plate, the Columbia River Basalt
221 Group (CRBG) is particularly rich in volatiles. 494,000 Gt of basalt produced during this period
222 is estimated to have resulted in 4,090-5,670 Gt of carbon release⁴³. This volcanic outgassing
223 contributed to the positive excursion in the $\delta^{13}\text{C}$ of atmospheric CO₂, increased CO₂ levels, and
224 caused global warming during the mid-Miocene. Such a scenario is supported by
225 reconstructions of seawater chemistry, which showed a major increase in dissolved inorganic
226 carbon in surface seawater due to the addition of volcanic CO₂ (Ref⁴⁴), as well as by climate-
227 biogeochemical cycle modelling⁴⁵. Interestingly, our results show that reduced OC burial in the
228 global ocean would act as an additional mechanism contributing to elevated CO₂ and therefore
229 global warming during the mid-Miocene (Fig. 4a, d, e).

230 Our global OC burial data can also be used together with estimates of carbonate burial⁴⁶
231 to evaluate the ratio between organic and inorganic carbon burial in the global ocean. Current
232 estimates of carbonate burial rely on a depth-dependent CaCO₃ preservation profile based on
233 carbonate compensation depth (CCD) reconstructions or mass balance for carbonate
234 alkalinity⁴⁶. Our calculated organic vs. inorganic burial ratio reaches a minimum during the
235 mid-Miocene, in particular, the Monterey period (Fig. 4g).

236 Assuming steady state in the long-term carbon cycle (Equation 1 and 2), we can also
237 evaluate the history of the carbon input flux during the Neogene. The carbon isotopic
238 composition of bulk organic matter⁴⁷ and carbonates⁴⁸ further enables us to compute the $\delta^{13}\text{C}$
239 of this carbon input. The calculated $\delta^{13}\text{C}$ of the carbon input shows large variations throughout
240 the Miocene, particularly during the mid-Miocene with a large positive shift from about 19 Ma,
241 peaking at around 14 Ma, with the calculated value from -5 to 0 ‰ (Fig. 4h). Similarly, the

242 calculated total flux of carbon input presents clear variations over the Neogene (Fig. 4g). These
243 substantial changes invoked for the carbon input and its isotopic values call for some
244 fundamental revisions of how we view the global carbon cycle through this period of Earth
245 history. Improved global carbon cycle models should be expected to include an organic sub-
246 cycle that is highly variable, and the amount and isotopic composition of total carbon input to
247 the surficial system should also evolve with time.

248 **OC burial as positive feedback for the global climate**

249 Although the controls on global OC burial are determined by many physical, chemical,
250 biological and geological conditions and the interactions between them, reduced burial during
251 the warmest phase of the past 23 million years might not be a coincidence. It is well known
252 that the temperature-dependent metabolic rates of heterotrophic bacteria result in high rates of
253 organic matter remineralization in a warmer water column, and therefore less carbon burial⁴⁹.
254 The metabolic activity of the microbes breaking down organic matter responds to temperature
255 dramatically, with metabolic rates doubling for every 10°C-temperature increase, known as the
256 Q10 pattern^{12, 13, 50}. Bacterial changes are much more sensitive to warming than photosynthesis
257 rates of primary producers, which leads to more efficient remineralization of sinking organic
258 matter and less OC buried in the sediments¹². Metabolic rate change has been invoked to
259 explain the elevated efficiency of organic matter recycling in warm climates and reduced OC
260 burial^{49, 51}.

261 The biological pump that is responsible for sending OC to the deep ocean, and ultimately
262 sediments, has been evaluated for its strength by using the depth habitat and stable isotopes of
263 planktonic foraminifera. Recent results suggest a much weaker biological pump during the
264 Eocene greenhouse climate⁵¹ and the warm mid-Miocene¹³. After 15 Ma, with the declining
265 temperatures of the ocean, the deep-dwelling planktonic foraminifera greatly expanded their
266 depth-habitat. These data, together with reconstructed $\delta^{13}\text{C}$ gradients in the water column and

267 an Earth System modeling, were used to reveal a 2-4 times increase in the particulate organic
268 matter flux to the mid-twilight zone over the past 15 million years¹³. This exemplifies how
269 changes in temperature-dependent metabolic rates have influenced the ocean carbon cycle,
270 consistent with our global OC burial data.

271 Our study quantitatively evaluates OC burial in the global ocean from the bottom-up, and
272 demonstrates unforeseen variability of this important component of the global carbon cycle.
273 The relationships between the organic carbon cycle and atmospheric CO₂ and O₂ levels are
274 understudied, as demonstrated by the mismatch between our findings and popular carbon cycle
275 models. Changes of OC burial over time as constrained by this study and future studies should
276 be incorporated into subsequent analyses of the global carbon cycle. Our results support the
277 notion that the greatly reduced OC burial during the warm period of the Miocene is related to
278 the temperature dependence of bacterial metabolism that remineralizes organic matter,
279 establishing positive feedback which increases atmospheric CO₂ as the climate warms. This
280 feedback mechanism is expected to operate during other warming intervals over Earth history,
281 as well as future warming of the global ocean.

282 **Acknowledgement** Acknowledgment is made to the donors of the American Chemical Society
283 Petroleum Research Fund (59797-DNI2 to Y.G.Z.) for support of this research. Z.Y.L.'s visit
284 to Texas A&M University was supported by the International Cooperative Program for
285 Innovative Talents through China Scholarship Council Grant No. 201600090202. B.J.W.M is
286 funded by the UK Natural Environment Research Council (NE/S009663/1). We thank Shuang
287 Zhang for helpful discussions, Johan Renaudie and Dave Lazarus at the Neptune Database by
288 providing biostratigraphy data for many sites used in this study, and John Dunne for providing
289 the modern OC burial data. We also acknowledge the International Ocean Discovery Program,
290 its funding agencies, and scientists around the world for generating the IODP data and making
291 it available. Y.G.Z. conceived this idea onboard IODP Expedition 363 and therefore

292 acknowledges the scientists and crew of that cruise, especially his fellow shipboard organic
293 geochemist Masanobu Yamamoto for their diligent work and stimulating conversations. We
294 thank the two anonymous reviewers for their thoughtful comments that helped to improve the
295 quality of this article.

296 **Author contributions** Y.G.Z. designed this study. Z.Y.L. collated, analyzed and interpreted the
297 data to establish OC burial records, with input from Y.G.Z. M.T. evaluated the records for
298 “Sadler Effect” and B.J.W.M. ran the carbon cycle models. All authors contributed to the
299 writing, led by Z.Y.L. and Y.G.Z.

300 **Competing interests** The authors declare that they have no competing interests.

301 **Correspondence and request for materials** should be addressed to Yi Ge Zhang
302 (yige.zhang@tamu.edu).

303 **Cited References**

304

305 1. Berner RA. Burial of organic carbon and pyrite sulfur in the modern ocean: Its geochemical and
306 environmental significance. *Am J Sci* 1982, **282**: 451-473.

307

308 2. Hedges JI, Keil RG. Sedimentary organic matter preservation: an assessment and speculative synthesis.
309 *Mar Chem* 1995, **49**: 81-115.

310

311 3. Broecker WS. A new boundary condition on atmospheric oxygen. *J Geophys Res* 1970, **75**: 3553-3557.

312

313 4. Garrels RM, Lerman A. Coupling of the sedimentary sulfur and carbon cycles - An improved model. *Am
314 J Sci* 1984, **284**: 989-1007.

315

316 5. Derry LA, France-Lanord C. Neogene growth of the sedimentary organic carbon reservoir.
317 *Paleoceanography* 1996, **11**: 267-276.

318

319 6. Kump LR, Arthur MA. Interpreting carbon-isotope excursions: carbonates and organic matter. *Chem
320 Geol* 1999, **161**: 181-198.

321

322 7. Mills BJW, Krause AJ, Scotese CR, Hill DJ, Shields GA, Lenton TM. Modelling the long-term carbon cycle,
323 atmospheric CO₂, and Earth surface temperature from late Neoproterozoic to present day. *Gondwana
324 Research* 2019, **67**: 172-186.

325

326 8. Krause AJ, Mills BJW, Zhang S, Planavsky NJ, Lenton TM, Poulton SW. Stepwise oxygenation of the
327 Paleozoic atmosphere. *Nat Commun* 2018, **9**: 4081.

328

329 9. Li G, Elderfield H. Evolution of carbon cycle over the past 100 million years. *Geochim Cosmochim Acta*
330 2013, **103**: 11-25.

331

332 10. Flower BP, Kennett JP. The middle Miocene climatic transition: East Antarctic ice sheet development,

333 deep ocean circulation and global carbon cycle. *Palaeogeogr Palaeoclimatol Palaeoecol* 1994, **108**: 537-
 334 555.

335

336 11. Vincent E, Berger WH. Carbon dioxide and polar cooling in the Miocene: The Monterey hypothesis. In: Sundquist ET, Broecker WS (eds). *The carbon cycle and atmospheric CO₂: Natural variations Archaen to Present*, vol. 32. AGU: Washington, DC, 1985, pp 455-468.

337

338

339 12. Regaudie-de-Gioux A, Duarte CM. Temperature dependence of planktonic metabolism in the ocean. *Global Biogeochem Cyc* 2012, **26**: GB1015.

340

341

342 13. Boscolo-Galazzo F, Crichton KA, Ridgwell A, Mawbey EM, Wade BS, Pearson PN. Temperature controls carbon cycling and biological evolution in the ocean twilight zone. *Science* 2021, **371**: 1148-1152.

343

344

345 14. Shields GA, Mills BJW. Tectonic controls on the long-term carbon isotope mass balance. *Proceedings of the National Academy of Sciences* 2017, **114**: 4318-4323.

346

347

348 15. Bolton EW, Berner RA, Petsch ST. The weathering of sedimentary organic matter as a control on atmospheric O₂: II. Theoretical modeling. *Am J Sci* 2006, **306**: 575-615.

349

350

351 16. Torres MA, West AJ, Li G. Sulphide oxidation and carbonate dissolution as a source of CO₂ over geological timescales. *Nature* 2014, **507**: 346-349.

352

353

354 17. Mason E, Edmonds M, Turchyn AV. Remobilization of crustal carbon may dominate volcanic arc emissions. *Science* 2017, **357**: 290-294.

355

356

357 18. Bradbury HJ, Turchyn AV. Reevaluating the carbon sink due to sedimentary carbonate formation in modern marine sediments. *Earth Planet Sci Lett* 2019, **519**: 40-49.

358

359

360 19. Schrag DP, Higgins JA, Macdonald FA, Johnston DT. Authigenic carbonate and the history of the global carbon cycle. *Science* 2013, **339**(540-543).

361

362

363 20. Gradstein FM, Ogg JG, Schmitz M, Ogg G. *The geological time scale* 2012. Elsevier, 2012.

364

365

366 21. Sadler PM. Sediment accumulation rates and the completeness of stratigraphic sections. *Journal of Geology* 1981, **89**: 569-584.

367

368

369 22. Berner RA. Examination of hypotheses for the Permo-Triassic boundary extinction by carbon cycle modeling. *Proc Natl Acad Sci* 2002, **99**: 4172-4177.

370

371

372 23. Pedersen TF, Calvert SE. Anoxia vs. productivity: What controls the formation of organic-carbon-rich sediments and sedimentary rocks? *AAPG Bulletin* 1990, **74**: 454-466.

373

374

375 24. Arthur MA, Sageman BB. Sea level control on source rock development: Perspectives from the Holocene Black Sea, the mid-Cretaceous Western Interior Basin of North America, and the Late Devonian Appalachian Basin. In: Harris NB (ed). *The deposition of organic carbon-rich sediments: Models, mechanisms and consequences*. Society for Sedimentary Geology: Tulsa, OK, 2005.

376

377

378

379

380 25. Hartnett HE, Keil RG, Hedges JI, Devol AH. Influence of oxygen exposure time on organic carbon preservation in continental margin sediments. *Nature* 1998, **391**: 572-574.

381

382

383 26. Lalonde K, Mucci A, Ouellet A, Gelinas Y. Preservation of organic matter in sediments promoted by iron. *Nature* 2012, **483**: 198-200.

384

385

386 27. Ingall EA, Van Cappellen P. Relation between sedimentation rate and burial of organic phosphorus and organic carbon in marine sediments. *Geochim Cosmochim Acta* 1990, **54**: 373-386.

387

388

389 28. Boyle RA, Dahl TW, Dale AW, Shields-Zhou GA, Zhu M, Brasier MD, *et al.* Stabilization of the coupled
390 oxygen and phosphorus cycles by the evolution of bioturbation. *Nature Geosci* 2014, **7**(9): 671-676.

391

392 29. Cartapanis O, Bianchi D, Jaccard SL, Galbraith ED. Global pulses of organic carbon burial in dee-sea
393 sediments during glacial maxima. *Nat Commun* 2016, **7**: 10796.

394

395 30. Longhurst AR. *Ecological geography of the sea*. . Elsevier, 2010.

396

397 31. Dunne JP, Hales B, Toggweiler JR. Global calcite cycling constrained by sediment preservation controls.
398 *Global Biogeochem Cyc* 2012, **26**: GB3023.

399

400 32. Kuehl SA, Hariu TM, Moore WS. Shelf sedimentation off the Ganges-Brahmaputra river system: Evidence
401 for sediment bypassing to the Bengal fan. *Geology* 1989, **17**: 1132-1135.

402

403 33. Wright LD, Freiedrichs CT. Gravity-driven sediment transport on continental shelves: A status report.
404 *Cont Shelf Res* 2006, **26**: 2092-2107.

405

406 34. Middlelburg JJ, Vlug T, Jaco F, Van der Nat W. Organic matter remineralization in marine systems. *Global*
407 *Planet Change* 1993, **8**: 47-58.

408

409 35. Shackleton NJ. The carbon isotope record of the Cenozoic: History of organic carbon burial and of oxygen
410 in the ocean and atmosphere. In: Brooks J, Fleet AJ (eds). *Marine petroleum source rocks*, vol. 26.
411 Geological Society Special Publication: London, UK, 1987, pp 423-434.

412

413 36. Compton JS, Snyder SW, Hodell DA. Phosphogenesis and weathering of shelf sediments from the
414 southeastern United States: Implications for Miocene $d^{13}C$ excursions and global cooling. *Geology* 1990,
415 **18**: 1227-1230.

416

417 37. John CM, Follmi KB, De Kaenel E, Adatte T, Steinmann P, Badertscher C. Carbonaceous and phosphate-
418 rich sediments of the Miocene Monterey Formation at El Capitan State Beach, California, U.S.A. *Journal*
419 *of Sedimentary Research* 2002, **72**: 252-267.

420

421 38. Follmi KB, Badertscher C, de Kaenel E, Stille P, John CM, Adatte T, *et al.* Phosphogenesis and organic-
422 carbon preservation in the Miocene Monterey Formation at Naples Beach, California-The Monterey
423 hypothesis revisited. *GSA Bull* 2005, **117**: 589-619.

424

425 39. Thomas E, Vincent E. Equatorial Pacific deep-sea benthic foraminifera: Faunal changes before the middle
426 Miocene polar cooling. *Geology* 1987, **15**: 1035-1039.

427

428 40. Tipple BJ, Meyers SR, Pagani M. Carbon isotope ratio of Cenozoic CO_2 : A comparative evaluation of
429 available geochemical proxies. *Paleoceanography* 2010, **25**: PA3202.

430

431 41. Hodell DA, Woodruff F. Variations in the strontium isotopic ratio of seawater during the Miocene:
432 Stratigraphic and geochemical implications. *Paleoceanography* 1994, **9**: 405-426.

433

434 42. Kasbohm J, Schoene B. Rapid eruption of the Columbia River flood basalt and correlation with the mid-
435 Miocene climate optimum. *Science Advances* 2018, **4**: eaat8223.

436

437 43. Lange RA. Constraints on the preeruptive volatile concentrations in the Columbia River flood basalts.
438 *Geology* 2002, **30**: 179-182.

439

440 44. Sosdian S, Babilia T, Greenop R, Foster G, Lear C. Ocean Carbon Storage across the middle Miocene: a
441 new interpretation for the Monterey Event. *Nat Commun* 2020, **11**(1): 1-11.

442

443 45. Longman J, Mills BJW, Donnadieu Y, Godderis Y. Assessing volcanic controls on Miocene climate change.
 444 *Geophys Res Lett* 2022, **49**: e2021GL096519.

445

446 46. Boudreau BP, Luo Y. Retrodiction of secular variation in deep-sea CaCO_3 burial during the Cenozoic. *Earth*
 447 *Planet Sci Lett* 2017, **474**: 1-12.

448

449 47. Falkowski PG, Katz ME, Milligan AJ, Fennel K, Cramer BS, Aubry M-P, et al. The rise of oxygen over the
 450 past 205 million years and the evolution of large placental mammals. *Science* 2005, **309**: 2202-2204.

451

452 48. Katz ME, Wright JD, Miller KG, Cramer BS, Fennel K, Falkowski P. Biological overprint of the geological
 453 carbon cycle. *Mar Geol* 2005, **217**: 323-338.

454

455 49. Olivarez Lyle A, Lyle M. Missing organic carbon in Eocene marine sediments: Is metabolism the biological
 456 feedback that maintains end-member climates. *Paleoceanography* 2006, **21**.

457

458 50. Stanley SM. Relation of Phanerozoic stable isotope excursions to climate, bacterial metabolism, and
 459 major extinctions. *Proceedings of the National Academy of Sciences* 2010, **107**: 19185-19189.

460

461 51. John EH, Wilson JD, Pearson PN, Ridgwell A. Temperature-dependent remineralization and carbon
 462 cycling in the warm Eocene oceans. *Palaeogeogr Palaeoclimatol Palaeoecol* 2014, **413**: 158-166.

463

464 **Fig. 1 | Location of our studied sites overlaid on the Longhurst biogeochemical provinces.**

465 The Longhurst map defines 56 coherent provinces from the modern biogeochemistry
 466 perspective³⁰, which were simplified to 27 provinces used in this study (Extended Data Table
 467 1). The original provinces were merged based on their geographical proximity and
 468 biogeochemical similarity, to ensure that each new province is represented by at least one site
 469 over the Neogene. Different shapes and colors denote IODP (International Ocean Discovery
 470 Program and Integrated Ocean Drilling Program, red diamonds), ODP (Ocean Drilling
 471 Program, maroon dots) and DSDP (Deep Sea Drilling Project, blue squares) sites.

472 **Fig. 2 | Provincial OC burial changes and their contribution to the global OC burial. a.**

473 Relative changes of provincial OC burial rates over time, with the “modern” (Pleistocene)
 474 value defined as 1; **b.** Provincial contribution to the global OC burial rates during the Neogene
 475 (total = 100%), with the leftmost column representing the modern burial of Dunne et al.³¹. The
 476 provinces presented here are identical to those shown in Fig. 1. Refer to Extended Data Table
 477 1 for the details of each province and the IODP sites used to construct provincial records.

478 **Fig. 3 | Neogene OC burial in the global ocean. a.** Burial rates calculated using different

479 definitions of provinces, including Longhurst (black curve with uncertainty envelope, $\pm 1\sigma$
480 in purple and $\pm 2\sigma$ in pale lilac), Oceans (blue curve), and FAO Fishing (orange curve)
481 approaches. **b.** Comparisons of global OC MAR between our record and the output of
482 commonly used global carbon cycle models (COPSE⁷, GEOCARBSULFOR⁸, and Li &
483 Elderfield⁹). All relative changes were normalized to the “modern” (Pleistocene) level.

484 **Fig. 4 | Neogene climate and carbon cycle changes.** **a.** A stacked deep-sea benthic
485 foraminiferal $\delta^{18}\text{O}$ curve⁵² **b.** Benthic $\delta^{13}\text{C}$ stack⁵². **c.** 3 Myr moving average of $\delta^{13}\text{C}_{\text{CO}_2}$ (Ref
486⁴⁰). **d.** Atmospheric CO_2 reconstructions based on marine proxies including the alkenone (green
487 hollow squares) and boron (solid blue squares) methods⁵³. Sky blue line is the LOESS fit curve.
488 **e.** Neogene OC burial in the global ocean with $\pm 1\sigma$ uncertainty envelope. **f.** Ratio between
489 organic carbon and carbonate carbon burial (OC: IC). Carbonate burial⁴⁶ was calculated based
490 on two CCD scenarios. **g.** Calculated flux of total carbon input to Earth’s surficial system.
491 Absolute burial rates were adjusted to match the assumption that the “modern” (2.5-0.5 Ma)
492 burial ratio between inorganic and organic carbon is 4:1. **h.** Calculated $\delta^{13}\text{C}$ of the total carbon
493 input to Earth’s surficial system. The changing inorganic vs. organic burial ratio during the
494 Neogene, together with $\delta^{13}\text{C}_{\text{IC}}$ (Ref⁴⁸) and $\delta^{13}\text{C}_{\text{org}}$ (Ref⁴⁷) data were used to obtain this record
495 though Equation 2. Pink and blue vertical bars highlight the timing of the Miocene Climatic
496 Optimum (MCO) and Middle Miocene Climate Transition (MMCT).

497

498 **Methods**499 **Methods Overview**

500 Building upon a study that reports global ocean OC burial variability since the last glacial period²⁹,
501 our calculation of global organic carbon burial fluxes over the Neogene (23.0-2.6 Ma) period
502 involves a series of consecutive steps. First, we screened 1508 sites from the Deep Sea Drilling
503 Project (DSDP, Leg 1-96), Ocean Drilling Program (ODP, Leg 100-210), Integrated Ocean Drilling
504 Program (IODP, Exp 301-312), and International Ocean Discovery Program (IODP, Exp 317-363).
505 Out of the 1,490 sites, 81 sites were identified (Fig. 1) with available total organic carbon
506 concentrations (TOC%), dry bulk density, and age model datums covering most of the past 23
507 million years. These sites span all major ocean basins and depositional environments, including
508 regions with large terrestrial sediment input, areas with strong upwelling activity and associated
509 high rates of primary productivity, and pelagic, carbonate-rich, open ocean areas, and so on.

510

511 The mass accumulation rates (MARs) of organic carbon (OC) were calculated for each site based
512 on sedimentation rate, bulk density, and TOC%. Individual TOC MARs were then used to determine
513 the spatial and temporal variability of regional and global OC burial in the Neogene. Extended Data
514 Fig. 8 provides an example to show the workflow of building TOC MARs from TOC%, bulk density
515 and age-depth relationship data.

516

517 To build the global burial OC fluxes from the 81 individual records, we subdivide the world ocean
518 into different biogeochemical provinces. The modern burial flux for each province, which is used
519 to scale our paleo-data, was estimated based on a series of algorithms and data from core-top
520 sediments and satellites⁵⁴. Given the inherent bias introduced by any such division, we employed
521 three different subdivision strategies (Fig. 1; Extended Data Fig. 5a, b) and compared the results to
522 assess the uncertainty of our global reconstruction.

523

524 Previous work has identified potential biases in flux reconstructions that make use of sedimentation
525 rate as a result of the Sadler Effect^{21, 55}. Simply, the inherent unsteadiness of depositional systems
526 results in a negative power-law relationship between measurements of sedimentation rate and the
527 amount of time averaged to determine the rate independent of the sedimentary depositional
528 environment²¹. To evaluate the potential impact of the Sadler Effect on our reconstruction, we
529 compared the averaging interval (duration of time between tie-points in an age model),

530 sedimentation accumulation, and OC burial for each record to determine the potential for spurious
531 patterns to arise in our global OC burial flux reconstruction (see section on Sadler Effect analysis
532 below).

533

534 **Site Selections**

535 Sediment cores from DSDP/ODP/IODP are our best archive for obtaining continuous records with
536 well-established chronology. Sediment from pelagic or hemipelagic sites would also, to some extent,
537 reduce the potential bias from turbidite sequences. We went through all Initial Reports volumes up
538 through IODP Expedition 363 to select sites suitable for this study.

539

540 Drilled sites must have sufficient quantity and quality of data to be included in our compilation,
541 with both complete or near complete sediment sections cored for the last 23 Myr, as well as a
542 reliable age model, TOC% and sediment bulk density data for the Neogene.

543

544 **Age Models**

545 Several independent approaches are often used by DSDP/ODP/IODP to provide constraints on the
546 chronology of sediment cores. These methods include biostratigraphy (planktonic foraminifer,
547 benthic foraminifer, calcareous nannofossils, diatoms, and radiolarians) and magnetostratigraphy
548 (geomagnetic polarity reversals). A major issue with age models published in the past few decades
549 is that they are based on different absolute timeframes of magnetic reversal or bio-horizon events.
550 Recent advances in radiometric dating, orbital tuning and the understanding of stratigraphic
551 relationships are reflected by the more recent Geological Timescale 2012 (GTS 2012) (ref. ²⁰). As
552 such, we converted all reported magnetochrons and microfossil biochronology at our study sites to
553 the GTS 2012 timescale so that comparisons between records and the stacking of records to obtain
554 a regional and global picture of OC deposition are referring to the same chronological framework.
555 Most of the IODP/ODP sites we used in this study have their age tie points readily available.
556 However, for sites where the initial reports and/or associated publications do not provide detailed
557 age-depth relationships (most DSDP sites), we consulted the Neptune database^{56, 57} to obtain the
558 biostratigraphic data.

559

560 **Sedimentation Rates**

561 Sedimentation rate for each site was determined by performing a 3rd-6th order polynomial regression
562 to the age-depth relationship (Extended Data Fig. 8), followed by the calculation of the first order

563 derivative of this relationship. Generally, the higher order of polynomial fitting would result in
 564 better fitting reflected by the r^2 values close to one. But we are aware of the possibility of over-
 565 fitting. Our strategy was that among all regressions with certain conditions (i.e., r^2 greater than 0.90
 566 and fitting residuals that do not vary systematically with age), the lowest order polynomial equation
 567 was selected to represent the age-depth relationship. Our polynomial regression captures these
 568 relationships well, reflected by the r^2 values from all sites ranging from 0.9185 to 0.9995 with a
 569 mean value of 0.9882 and 1σ of ± 0.0015 .

570

571 **Dry Bulk Density and TOC%**

572 Dry bulk density (DBD) measurements are performed by shipboard physical property specialists,
 573 with the data presented in the “Physical Properties” section of the initial site reports. TOC% are
 574 determined by shipboard geochemists. These data are published in “Geochemistry”, “Organic
 575 Geochemistry” or “Carbon Geochemistry” section of the initial site reports. They are available as
 576 tables associated with the site report or can be found online through the “Janus” database for
 577 Expedition 1-312, or the “LIMS” database for Expedition 317 - present. Because some DSDP sites
 578 only reported bulk density (BD) but not dry bulk density data, we developed an empirical equation
 579 with statistical significance based on a linear correlation between DB and DBD ($R^2 = 0.9995$), using
 580 842 data points from 10 IODP sites where both type of measurements are available:

$$581 \text{DBD} = 1.5441 \times \text{BD} - 1.5458 \quad \text{Equation 3}$$

582

583 **The Quality of IODP's TOC% Data**

584 DSDP/ODP/IODP use a standard “subtraction” method onboard of the R/V to determine TOC%,
 585 which is based on the differences between the total carbon measured by a CHNS elemental analyzer
 586 (EA) and the inorganic carbon measured by a coulometer. This method is generally considered to
 587 be accurate. For example, Meyers and Silliman⁵⁸ replicated the ship-board TOC% measurements
 588 by performing shore-based experiments that removed the carbonate fraction of samples through
 589 acid digestion (i.e., “acidification method”). The residues were then washed, dried, and measured
 590 on an EA. Their shore-based results (0.06-3% TOC) were positively correlated with the shipboard
 591 values⁵⁸. However, Olivarez Lyle and Lyle⁵⁹ argued that the subtraction method introduces large
 592 errors when TOC% is low (< 0.3%). By using carefully designed acid digestion method, Olivarez
 593 Lyle and Lyle⁴⁹ were able to report very low mean TOC concentrations of about 0.03% at Sites
 594 1218 and 1219, levels that are “below detection” using the standard subtraction method⁶⁰. In this
 595 case, acidification method clearly showed its advantage over the standard subtraction method when

596 sediment samples bear very low TOC%. However, samples reportedly have “0%” or “below
 597 detection” of TOC constitutes only 2.5% of our database.

598

599 Several IODP publications attempted to evaluate of the accuracy of the standard “subtraction”
 600 method for determining TOC%^{61, 62}. Here, we compiled all available TOC% data that have been
 601 constructed from both the “subtraction” and “acidification” methods and compare them downcore
 602 as well as scatter plot on the absolute abundance scale (Extended Data Fig. 1). Some offsets between
 603 the two datasets were observed. Nevertheless, the overall relationship suggests that the two
 604 independent methods yield comparable results (p -value = 1.38×10^{-17}), supporting the robustness of the
 605 standard subtraction method for TOC% used by IODP.

606

607 Also, to determine the consistency of TOC% data reported by DSDP, ODP or IODP expeditions
 608 over several decades, we compared results found in nearby locations. To obtain more material for
 609 follow up studies, IODP expeditions occasionally revisit earlier DSDP or ODP site locations. Since
 610 their locations and water depth are almost identical, a direct comparison of TOC% on the depth
 611 scale of these sites was conducted (Extended Data Fig. 2). When the sites were not directly
 612 “revisited” but still drilled within a short distance and similar water depth, we used a criterion of
 613 <10 km apart and <200 m depth differences to identify sites suitable for such comparisons, with
 614 one exception of IODP U1341 and DSDP 188 that are slightly further apart but still bearing similar
 615 physical properties. For sites that are beyond this range, substantially different sedimentation rates
 616 would complicate any TOC% comparison on the depth scale. Extended Data Fig. 2 shows a broad
 617 agreement between DSDP, ODP and IODP-derived TOC% results, except for the Sites 716 - U1467
 618 where the ODP results constantly represent the lower end of the IODP measurements. The
 619 resemblance of TOC% records from nearby sites but measured during different time periods
 620 demonstrates the long-term consistency of IODP’s TOC% data.

621

622 OC MAR Calculations

623 Mass accumulation rate (MAR) of OC is calculated by the equation:

$$624 \text{TOC MAR} = \text{SR} \times \text{TOC\%} \times \text{DBD} \quad \text{Equation 4}$$

625 Where SR (cm kyr^{-1}) is the sedimentation rate, TOC% is the weight percentage of total organic
 626 carbon, and DBD is the dry bulk density (g cm^{-3} , grams of sediment per cubic centimeter of the
 627 original wet sample). If TOC% and DBD are not from the identical set of samples, then DBD data
 628 were interpolated to the depth of the TOC% data since DBD data usually have a higher sampling

629 density. Extended Data Fig. 8 presents a working flow chart of IODP Site U1337, as an example to
630 show how OC MAR data were obtained.

631

632 **Sadler Effect Analysis**

633 Apparent variations in sedimentation rate due to changes in the averaging interval (i.e., the duration
634 of time between points in the age-depth relationship used to calculate sedimentation rate²¹) might
635 contribute noise and/or bias in our reconstruction of OC MAR. If, for example, more recent portions
636 of the core were characterized by higher resolution dating, then this could manifest as an artifactual
637 increase in OC MAR due to differences in the averaging interval between younger and older
638 portions of the record.

639

640 To assess whether changes in the averaging interval influence our ultimate conclusions about OC
641 burial, we computed the expected changes in OC MAR that arise solely from changes in the
642 averaging interval (i.e., the Sadler Effect) and compared these to our observations (Extended Data
643 Fig. 3). To calculate the averaging interval for each depth in each core where we have an estimate
644 of OC MAR, we identified the closest (in depth) age determinations above and below the OC MAR
645 measurement and took the difference in age as a measure of the averaging interval. Using the power-
646 law exponent for the relationship between averaging interval and sedimentation rate in Sadler
647 (1981), we calculated a relative sedimentation rate for each measurement of OC MAR in each core.
648 Using the same extrapolation algorithm used to calculate a global OC MAR (see below), we
649 determine a global estimate of relative changes in sedimentation rate due solely to differences in
650 the averaging interval with time. This time-series represents the pattern of changes in OC MAR
651 that could arise artifactualy.

652

653 In panels a and b of Extended Data Fig. 3, we show the range in averaging timescale between each
654 core for a given age bin (i.e., the raw data used in the global extrapolation). This analysis shows a
655 slight decrease in averaging interval towards the present (Extended Data Fig. 3a). However,
656 differences in the distribution of averaging intervals between three time bins picked to capture the
657 general U-shape trend in global OC MAR are too small to explain the factor of 2 changes in OC
658 MAR apparent in our global reconstruction (Extended Data Fig. 3b). This result, along with the
659 evidence that TOC%, and not sedimentation rate, is the dominant control on OC MAR for most
660 sites (Extended Data Fig. 10), suggests that the patterns in our global OC MAR reconstruction
661 reflect real changes during the Neogene and not solely spurious artifacts having to do with the

662 complexities of the sedimentary record. This conclusion is further supported by comparing the
663 global record of OC MAR to the global record expected based on spurious changes in sedimentation
664 rate (Extended Data Fig. 3c, d). The poor correlation between the observations and the predictions
665 using the Sadler Effect support the conclusion that the general U-shaped trend in OC MAR is a
666 primary signal.

667

668 **Apparent Controls of OC MARs**

669 Geographically, regions like the Southwest African continental margin, Northwest Atlantic
670 Ocean, Bay of Bengal, Antarctica margin (Wilkes Land) and Peru continental margin appear
671 to be OC burial “hot spots” (Extended Data Fig. 4). Highly productive open ocean settings (e.g.,
672 upwelling regions in the eastern equatorial Pacific) do not show particularly high OC burial
673 (Extended Data Fig. 4). In contrast, coastal-upwelling areas with high productivity and ample
674 supply of terrigenous material have the ideal conditions for high OC burial rates¹, as
675 exemplified by the Southwest African continental shelf and Peru continental margin. In the
676 Bay of Bengal, high erosion rates of the Himalayas provided large amount of terrestrial organic
677 matter and clastic material^{63, 64}, resulting in high sedimentation rate and rapid accumulation of
678 OC (Extended Data Fig. 4). Of course, the geographical pattern discussed here are restricted
679 spatially and temporally by the available IODP records with high quality and continuous TOC
680 MAR records. Consequently, these records were used to scale for regional OC burial changes
681 (Fig. 2) which reduces the sensitivity of calculated regional and global OC burial to any
682 individual TOC MAR record.

683

684 To evaluate the apparent controlling factor of OC burial, we performed simple liner regression
685 fittings between MAR and SR, TOC%, and DBD of each site. Importantly, SR and TOC% are
686 interdependent – for example, rapid sedimentation dilutes OC flux, whereas quick burial potentially
687 reduces the exposure time of OC to oxygen and therefore enhances the preservation of organic
688 matter. Our analysis does not distinguish between these interconnections. The most significant
689 correlation exhibited by the highest r^2 value was identified (Extended Data Fig. 9). The fitting
690 results showed that TOC% exerts the largest control (68% of the sties) on MARs. In addition, 13.5%
691 of the sites had OC MAR that were primarily influenced by changes in SR. Unclear controls were
692 found in 18.5% of sites, implying a mixed influence. Our results show that TOC content appears to
693 exert the dominant control of OC burial in a large number of sites, although TOC% itself is
694 impacted by SR (Extended Data Fig. 9).

695

696 **Provincial Definition Strategies**

697 To infer regional/global patterns of OC burial changes from individual sites, we subdivided the
 698 world ocean into different sets of geographical provinces. Given the inherent bias introduced by
 699 any such subdivision, we adopted three different subdivision strategies (Fig. 1; Extended Data Fig.
 700 5) and compared the results to test the dependence of our results on provincial definition.

701

702 Since the modern configuration of continents and oceans are largely in place during the Neogene,
 703 we utilized the Longhurst biogeochemical provinces of the modern ocean, assuming that the large-
 704 scale ocean features driving biogeochemical cycles have remained relatively stationary over time.
 705 The Longhurst biogeochemical map defines 56 coherent provinces, which was simplified into 27
 706 provinces in our study (Extended Data Table 1) to adapt the ocean delineation to our site distribution.

707

708 To test how reliable regional and global OC burial records based on the Longhurst provinces are,
 709 we explored two other definitions. Very simply, we used the Arctic, Atlantic (South and North),
 710 Indian, Pacific (North, South, and Western) and Southern Oceans (Extended Data Fig. 5a),
 711 according to IHO Sea Areas, with version 3 retrieved from <http://www.marineregions.org/>. Another
 712 method is from FAO “Major Fishing Areas for Statistical Purposes”, with the shapefiles retrieved
 713 from the FAO Fisheries and Aquaculture Department website,
 714 <http://www.fao.org/fishery/area/search/en>. FAO subdivided the Atlantic and Pacific Oceans into
 715 northwest, northeast, western central, eastern central, southwest, southeast and Antarctic regions.
 716 Also, the Indian Ocean was subdivided into western, eastern and Antarctic and Southern regions.
 717 Since there were no suitable sites for the Mediterranean and Black Sea, we combined the two areas
 718 into one conjoined province. Mercator projection for maps were used in both GMT and R.

719

720 **Potential Water Depth Influence**

721 As oceanic crusts move away from the spreading center (i.e., middle ocean ridges), they sink
 722 progressively. This implies that almost all our studied sites would be in shallower water depth
 723 during the Neogene than they are today. Using an observation-based empirical relationship ($D =$
 724 $320 \times \sqrt{\text{Age}}$, where ‘D’ is depth added and ‘Age’ is in million years) that is widely accepted⁶⁵,
 725 sites are estimated to be ~1,500 m shallower at 23 Ma. However, the relationship between water
 726 depth and OC burial rates is complicated and nonlinear. This is exemplified by analyses of our

727 “modern” (Pleistocene) OC burial rates from the 81 sites and their modern water depth, which does
 728 not show any significant correlation. The linear regression yields result with $r^2 = 0.00000002$ and $p = 0.999$. Also, in contrast to time-induced water depth change that is monotonic, our reconstructed
 729 global OC burial record shows overall high, low and then high rates of organic burial over the
 730 Neogene (Fig. 3), arguing against a general water-depth control. Although the influence of water
 731 depth changes on our OC burial records is difficult to quantify, our approach of using one or more
 732 TOC MAR record(s) to scale for provincial changes helps to alleviate this potential issue. For 27
 733 biogeochemical provinces used in this study, 21 of them have more than one TOC MAR record,
 734 often representing sites from different water depths (Extended Data Table 1).

736

737 **Calculations of Regional and Global OC Burial**

738 Modern OC burial in the global ocean with a $1 \times 1^\circ$ spatial resolution of Dunne et al.^{31, 54} is the basis
 739 for our modern provincial OC burial rates, obtained from areal integrals of all data points within
 740 that province (Extended Data Fig. 6). This modern OC burial map is produced by a series of data
 741 and algorithms considering satellite-based primary production, particulate organic matter
 742 generation, transportation and burial in the sediments, which leads to a global burial of ~ 0.146 Gt
 743 C yr^{-1} (Ref^{31, 54}). However, different methods have yielded drastically estimates of modern burial,
 744 possibly due to the fact that core-top samples could carry signals that are tens of thousands of years
 745 old but the sedimentation/remineralization rates were poorly constrained⁶⁶. Nonetheless, recent
 746 studies utilized ^{230}Th -normalized fluxes to tackle this issue by minimizing age model uncertainties.
 747 For example, Hayes et al.⁶⁷ compiled results from 12,000 globally distributed marine cores and
 748 1,068 flux estimates of the deep ocean. Their reported “deep water” ($>2,000$ m) annual OC burial
 749 of 0.017 ± 0.005 Gt C yr^{-1} is much more in line with Dunne et al. (2007, 2012) deep water burial
 750 rate of 0.012 Gt C yr^{-1} , supporting the robustness of the modern OC burial map used in this study.

751

752 Next, the ratio between TOC MARs of any Neogene interval and “Modern” (Pleistocene) of each
 753 site was calculated. If there are more than one site from any province, then these OC burial records
 754 were averaged to obtain the composite provincial changes. Subsequently, the absolute modern
 755 burial value of each province is multiplied by these ratios to determine provincial changes of OC
 756 burial over time. Finally, the sum of all provincial OC burial data provides the global OC
 757 accumulation rates. Mathematically, this approach can be written down as:

$$758 \text{OC Burial}_{(t)} = \sum_{p=1}^{27} m_p \cdot (\overline{OCV}_{s,t} \mid s \in p) \quad (\text{Equation 6})$$

759 where global OC burial at time t is the sum over all 27 provinces (Fig. 1, Extended Data Table 1)

760 and OC burial in each province (p) is determined by the mean OC variability (OCV, with “modern”
 761 or 2.5-0.5 Ma defined as ‘1’) across all sites (s) within the province at the time t, multiplied by its
 762 modern provincial burial (m_p) (Extended Data Table 1). This approach also allows for easy
 763 adjustments if our understanding of the modern global burial further improves in the future.

764

765 For calculated global OC burial, the following equation was used to estimate the errors:

$$766 f = \sum_i^n a_i \sigma_{\bar{i}} \quad \text{Equation 7}$$

767 Where $\sigma_{\bar{i}}$ is the standard error of the OC burial change rate of each province, a is the modern
 768 provincial burial. Since modern OC burial values for each province are uncorrelated, the variance
 769 of f is therefore:

$$770 \sigma_f^2 = \sum_i^n a_i^2 \sigma_{\bar{i}}^2 \quad \text{Equation 8}$$

771 where

$$772 \sigma_f = \sqrt{\sum_i^n a_i^2 \sigma_{\bar{i}}^2} \quad \text{Equation 9}$$

773

774 **Extended Data Fig. 1 | Comparisons of TOC% obtained by “subtraction” method and**
 775 **“acidification” method.** **a-c.** ODP Sites 897-899. **d.** IODP Site U1482. Navy blue squares are
 776 the measurements on board by subtraction between total and carbonate carbon contents, while
 777 blue dots are from the acidification method direct measured from carbonate-free samples. **e.**
 778 Linear regression of TOC contents determined by two independent methods. The regression
 779 equation is expressed as $y = 0.8653*x$, with $R^2 = 0.523$, $p\text{-value} = 1.38\text{e-}17$ and $\text{RMSE} = 0.593$,
 780 suggesting a significant linear relationship at the 0.05 level of significance. The dashed grey
 781 line indicated the one-to-one correspondence of the two variables.

782

783 **Extended Data Fig. 2 | Comparisons of TOC% reported by DSDP, ODP or IODP**
 784 **expeditions from nearby locations.** **a.** IODP U1513 vs DSDP 258. **b.** IODP U1417 vs DSDP
 785 178. **c.** IODP U1467 vs ODP 716. **d.** IODP U1327 vs ODP 889A. **e.** IODP U1341 vs DSDP
 786 188. **f.** IODP U1424 vs ODP 794. **g.** ODP 904 vs DSDP 612. Site details are shown in
 787 Supplemental Data 10.

788

789 **Extended Data Fig. 3 | Sadler effect evaluation.** **a.** Changes in averaging intervals and their
 790 ranges between cores for 1 Ma time bins. The large black points show median values. The

791 vertical black lines show the range from minimum to maximum averaging interval. The small
792 grey points show the averaging intervals for individual cores in each time bin. The colored
793 horizontal lines show the mean values for 3 age bins selected to capture the general U-shaped
794 trend in OC MAR. **b.** Probability density functions of averaging intervals calculated for each
795 core grouped into three age bins (>17.5 Ma, 10-17.5 Ma, and 2.5 to 10 Ma). **c.** Time-series of
796 relative changes in global OC MAR (black) and global averaging interval (blue) expressed as
797 a sedimentation rate using the power-law scaling of Sadler (1981). **d.** Scatter plot of global OC
798 MAR and the global averaging interval expressed as a sedimentation rate showing a poor
799 correlation.

800

801 **Extended Data Fig. 4 | Individual site TOC MARs over four time slices during the**
802 **Neogene.** **a.** 20 Ma (early Miocene), **b.** 15 Ma (middle Miocene), **c.** 10 Ma (late Miocene), and
803 **d.** 5 Ma (early Pliocene). Paleogeographic maps were reconstructed using Gplates software⁶⁸,
804 with the sites rotated back to their paleo-locations. The contours of OC burial rate were
805 obtained by performing IDW (Inverse distance weight function) interpolation of the data from
806 individual sites (black dots, see Fig. 1 for site labels).

807

808 **Extended Data Fig. 5 | Alternative approaches to define provinces of the world's ocean.** **a.**
809 IHO Sea Areas provinces. According to the IHO Sea Areas provinces zoning method, the global
810 ocean is divided into the Arctic, Atlantic, Indian, Pacific and Southern Oceans. The Atlantic
811 and Indian Oceans are further divided into the North and South Atlantic and the South, North
812 and West Pacific, resulting in a total of 8 provinces. **b.** FAO Fishing Areas provinces. This
813 method divides the global ocean into 19 geographical regions. Different shapes and colors
814 indicate IODP (red diamonds), ODP (maroon dots), and DSDP (blue squares) site locations.

815

816 **Extended Data Fig. 6 | "Modern" OC burial rates of the global ocean.** The map was
817 generated by data from Dunne et al. (2007, 2012). Also shown are "modern" (Pleistocene)
818 burial rates of our 81 IODP sites (in diamond squares) color coded with the same scheme of
819 the Dunne map.

820

821 **Extended Data Fig. 7 | Comparing OC burial rates of different locations over several**
822 **stages of the "Monterey period".** OC accumulation rates for the Monterey Formation (EL
823 Capitan) are compared with sites from the eastern equatorial Pacific (EEP, Site 1338), Bay of

824 Bengal (Site U1451), Southwest African continental Shelf (Site 362) and open ocean (Site
825 1335). Note that OC burial rates for the Monterey Formation are generally higher than the open
826 ocean site, but lower than other sites.

827

828 **Extended Data Fig. 8 | An example to show how OC MAR is calculated (Site U1337).** A
829 flow chart that uses data from Site 1337 as an example to illustrate the procedures of deriving
830 the sedimentation rate (**b**) from the age-depth relationship (**a**), together with the TOC% and dry
831 bulk density data (**c**) to produce the (**d**) TOC mass accumulation rate (MAR).

832

833 **Extended Data Fig. 9 | Controlling factors for OC burial in our studied sites.** **a.** map
834 shows either TOC% or sedimentation rate (SR) control on OC burial rates of each site. **b.** A
835 histogram to present the number and percentage of sites controlled by either TOC%, or SR,
836 as well as the ones with unclear relationships.

837

838 **Extended Data Table 1 | Information of the modified Longhurst biogeochemical**
839 **provinces used in this study and their associated TOC MARs records.**

840

841 **Supplemental Data File 1 | Site information and TOC MARs.**

842

843 **Supplemental Data File 2 | Longhurst biogeochemical province information and their**
844 **modern/Neogene OC burial.**

845

846 **Supplemental Data File 3 | IHO ocean zonation information and their modern/Neogene**
847 **OC burial.**

848

849 **Supplemental Data File 4 | FAO ocean zonation information and their modern/Neogene**
850 **OC burial.**

851

852 **Supplemental Data File 5 | IODP sites paleogeography and visualization of their TOC**
853 **MARs over the Neogene.**

854

855 **Supplemental Data File 6 | Neogene global OC burial changes according to carbon cycle**
856 **models.**

857

858 **Supplemental Data File 7 | Calculations of the flux and isotopic value of Neogene carbon**
859 **input into the surficial system.**

860

861 **Supplemental Data File 8 | Linear fitting results between TOC MARs and SR, TOC%,**
862 **and DBD of each site.**

863

864 **Supplemental Data File 9 | Sadler effect evaluation.**

865

866 **Supplemental Data File 10 | Location, water depth and distance of sites used in Extended**
867 **Data Fig. 2.**

868

869

870 **Data Availability**

871 All individual site, regional and global OC burial data, calculations for region and global OC
872 burial rates and the Neogene global carbon cycle are available at Figshare
873 (<https://doi.org/10.6084/m9.figshare.21001849>). These data are also archived as
874 Supplementary Data Files (1-10) associated with the online version of this article.

875

876 **Code Availability**

877 The algorithm used to calculate regional and global OC burial from TOC MAR of individual
878 sites is publicly available as MATLAB and R code package on GitHub
879 (<https://github.com/Ziyeli-moc/OC-burial.git>).

880

881

882 **Cited References**

883

884

885

52. Zachos JC, Dickens GR, Zeebe RE. An early Cenozoic perspective on greenhouse warming and carbon-
886 cycle dynamics. *Nature* 2008, **451**: 279-283.

887

888

889

53. Rae JWB, Zhang YG, Liu X, Foster GL, Stoll HM, Whiteford RDM. Atmospheric CO₂ over the past 66 million
years from marine archives. *Annu Rev Earth Planet Sci* 2021, **49**: 609-641.

890

891

892

54. Dunne JP, Sarmiento JL, Gnanadesikan A. A synthesis of global particle export from the surface ocean
and cycling through the ocean interior and on the seafloor. *Global Biogeochem Cycles* 2007, **21**: GB4006.

893

894

895

55. Molnar P, England P. Late Cenozoic uplift of mountain ranges and global climate change: Chicken or egg?
Nature 1990, **346**: 29-34.

896

897

898

56. Lazarus DB. Neptune: A marine micropaleontology database. *Mathematical Geology* 1994, **26**: 817-832.

899

900

57. Spencer-Cervato C. The Cenozoic deep sea microfossil record: Explorations of the DSDP/ODP sample set
using the Neptune database. *Palaeontologia electronica* 1999, **2**: 270.

901

902 58. Meyers PA, Silliman JE. Organic matter in Pleistocene to Quaternary turbidites from Sites 897, 898, 899
903 and 900, Iberia Abyssal Plain. In: Whitmarsch RB, Sawyers DS, Klaus A, Masson DG (eds). *Proceedings of*
904 *the Ocean Drilling Program, Scientific Results*, vol. 149. Ocean Drilling Program: College Station, TX, 1996,
905 pp 305-313.

906

907 59. Olivarez Lyle A, Lyle M. 20. Organic carbon and barium in Eocene sediments: Possible controls on
908 nutrient recycling in the Eocene equatorial Pacific Ocean. In: Wilson PA, Lyle M, Firth JV (eds).
909 *Proceedings of the Ocean Drilling Program, Scientific Results*, vol. 199. Ocean Drilling Program: College
910 Station, TX, 2005, pp 1-33.

911

912 60. Shipboard Scienfitic Party. 12. Site 1219. In: Lyle M, Wilson PA, Janecek TR (eds). *Proceeding of the Ocean*
913 *Drilling Program, Initial Reports*, vol. 199. Ocean Drilling Program: College Station, TX, 2002.

914

915 61. Expedition 306 Scientists. Site U1312-U1315 methods. In: Channell JET, Kanamatsu T, Sato T, Alvarez
916 Zarikian CA, Malone MJ, the Expedition 303/306 Scientists (eds). *Proceedings of the Integrated Ocean*
917 *Drilling Program*, vol. 303/306. IODP: College Station, TX, 2006.

918

919 62. Expedition 317 Scientists. Methods. In: Fulthorpe CS, Hoyanagi K, Blum P, the Expedition 317 Scientists
920 (eds). *Proceedings of the Integrated Ocean Drilling Program*, vol. 317. IODP: College Station, TX, 2011.

921

922 63. Galy V, France-Lanord C, Beyssac O, Faure P, Kudrass H, Palhol F. Efficient organic carbon burial in the
923 Bengal fan sustained by the Himalayan erosional system. *Nature* 2007, **450**: 407-410.

924

925 64. France-Lanord C, Derry LA. Organic carbon buria forcing of the carbon cycle from Himalayan erosion.
926 *Nature* 1997, **390**: 65-67.

927

928 65. Sclater JG, Anderson RN, Bell ML. Elevation of ridges and evolution of the central eastern Pacific. *J*
929 *Geophys Res* 1971, **76**: 7888-7915.

930

931 66. Burdige DJ. Preservation of organic matter in marine sediments: controls, mechanisms, and an
932 imbalance in sediment organic carbon budgets? *Chemical Reviews* 2007, **107**: 467-485.

933

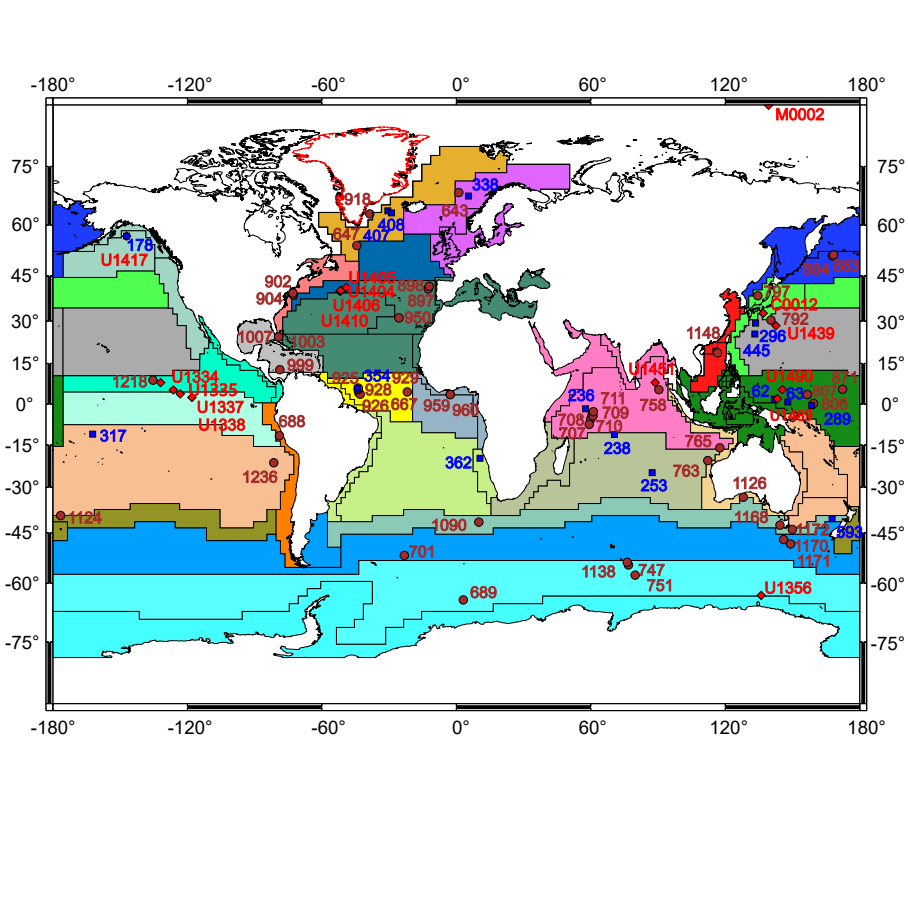
934 67. Hayes CT, Costa KM, Anderson RF, Calvo E, Chase Z, Demina LL, *et al.* Global Ocean sediment
935 composition and burial flux in the deep sea. *Global Biogeochem Cyc* 2021, **35**: e2020GB006769.

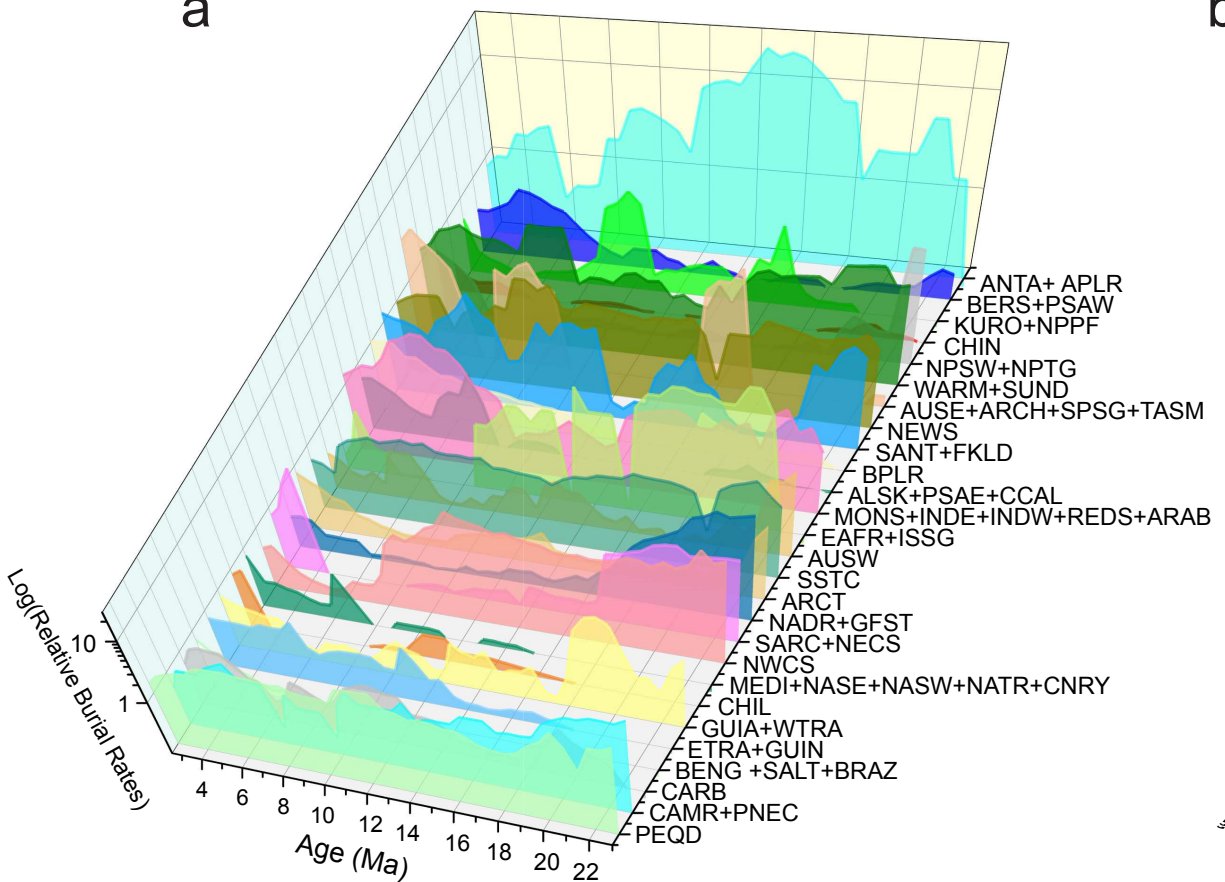
936

937 68. Muller RD. GPlates: Building a virtual Earth though deep time. *Geochem Geophys Geosyst* 2018, **19**:
938 2243-2261.

939

940



a**b**